Epitaxial Transition from Gyroid to Cylinder in a Diblock Copolymer Melt

Takashi Honda*

Japan Chemical Innovation Institute and Department of Organic and Polymeric Materials, Tokyo Institute of Technology, Ookayama, Meguro-ku, Tokyo 152-8552, Japan

Toshihiro Kawakatsu

Department of Physics, Tohoku University, Aoba, Aramaki, Aoba-ku, Sendai 980-8578, Japan

Received September 23, 2005; Revised Manuscript Received January 2, 2006

ABSTRACT: An order−order transition from a bicontinious double-gyroid (G) structure to a hexagonally packed cylinder (C) structure induced by an external flow is simulated by using real-space dynamical self-consistent field technique. To simulate the structural change correctly, we introduce a system size optimization technique by which emergence of artificial intermediate structures are suppressed. When a shear flow in [111] direction of the G unit cell is imposed, a nucleation of the C domains followed by a stable coexistence between the G phase and the C phase is observed. We confirm that the generated C domains grow epitaxially, where the {220} planes of the G structure coincide with the {10} planes of the C structure (so-called epitaxial growth), while the experimental studies suggest {211} to {10} transition. In a steady state under the shear flow, the G structure shows different splitting and reconnection processes when the direction of the velocity gradient of the shear flow is changed. Thus, the kinetic pathway from the initial G phase to the final C phase is determined, not only by the commensurability between the positions and the lattice constants of the initial and the final domain structures (epitaxial condition), but also by the stability of the phase coexistence that depends on the direction of the velocity gradient.

1. Introduction

In the past, the self-organized microdomain structures of diblock copolymers have been the target of extensive studies, both experimentally and theoretically.[1−6] It is well-known that the block copolymers show typical microdomain structures, such as the body-centered cubic crystal of spherical domains (S), hexagonally packed cylinders (C), lamellar domains (L), and bicontinuous double-gyroid (G) structures. In predicting the equilibrium phase diagram of the block copolymers, the mean-field theories, such as the Ginzburg−Landau type model with the random phase approximation (RPA) and the self-consistent field (SCF) theory, are quite useful and have played a very important role. By using these mean-field theories, one can evaluate the stability of each of the microdomain structures[1,7−9] from which the phase diagram is constructed. Such a theoretical phase diagram was actually confirmed by experiments.[10]

Among various microdomain structures, the G structure has attracted a great deal of interest because of its complex but highly symmetric structure (space group $Ia\bar{3}d$).[11] In Figure 1, we show an equilibrium G structure calculated by using our SCF method, whose detail will be described in the next section. Taking advantage of its complex domain structure, the G structure is expected to have a wide applicability to various techniques, for example, three-dimensional (3D) photonic crystals, microporous systems, nanoreactors, and so on.[12−15]

Despite the success in the understanding of the equilibrium phase behaviors, many of the problems on the dynamical properties are still open. Typical examples are the order−order transitions (OOTs) and the order−disorder transitions (ODTs) between the microdomain structures of blockcopolymers induced by changing the temperature or by imposing an external field such as a flow field or an electric field. For example, the G phase can easily be transformed into the C phase or to the L phase by a temperature jump or by an external shear flow because these phases are neighboring on the phase diagram separated by first-order phase transition lines.[16] In the present study, we simulate the OOT G → C by using a dynamical extension of the SCF theory.

One of the simplest and the most popular techniques used in studying the OOTs and ODTs theoretically is the time-dependent Ginzburg−Landau (TDGL) model, where only the leading few terms in the power series expansion of the free energy with respect to the composition fluctuations are retained. The TDGL theory was used to investigate the instability in the OOTs and ODTs between S, C, and L structures[17] and the transitions G → C and C → L.[18,19] Although the TDGL theory has an advantage that it can treat large-scale systems, it is, in principle, valid only in the weak segregation regime because of the use of the power series expansion. However, if one is interested in the G phase, the TDGL theory becomes less accurate because the G phase exists only in the intermediate segregation regime. The SCF theory is the technique that can be used to study the phase transitions up to the strong segregation regime with a quantitative accuracy. This is due to the direct and precise numerical evaluation of the conformational entropy of the polymer chains in the SCF calculation.[7,20−22] By using the SCF theory, the OOTs L ↔ C, C ↔ S, and G → C have been investigated.[23−25] By using a similar technique, Matsen proposed a model of the nucleation and growth process of the epitaxial OOT G → C.[24,25]

On the experimental side, the so-called "epitaxial domain growth" has been one of the central issues in the discussions on the OOTs of block copolymers because such a growth

* Corresponding author. E-mail: thonda@polymer.titech.ac.jp. Telephone: +81-3-5734-2632. Fax: +81-3-5734-2888.

10.1021/ma052075z CCC: $33.50
Published on Web 02/23/2006

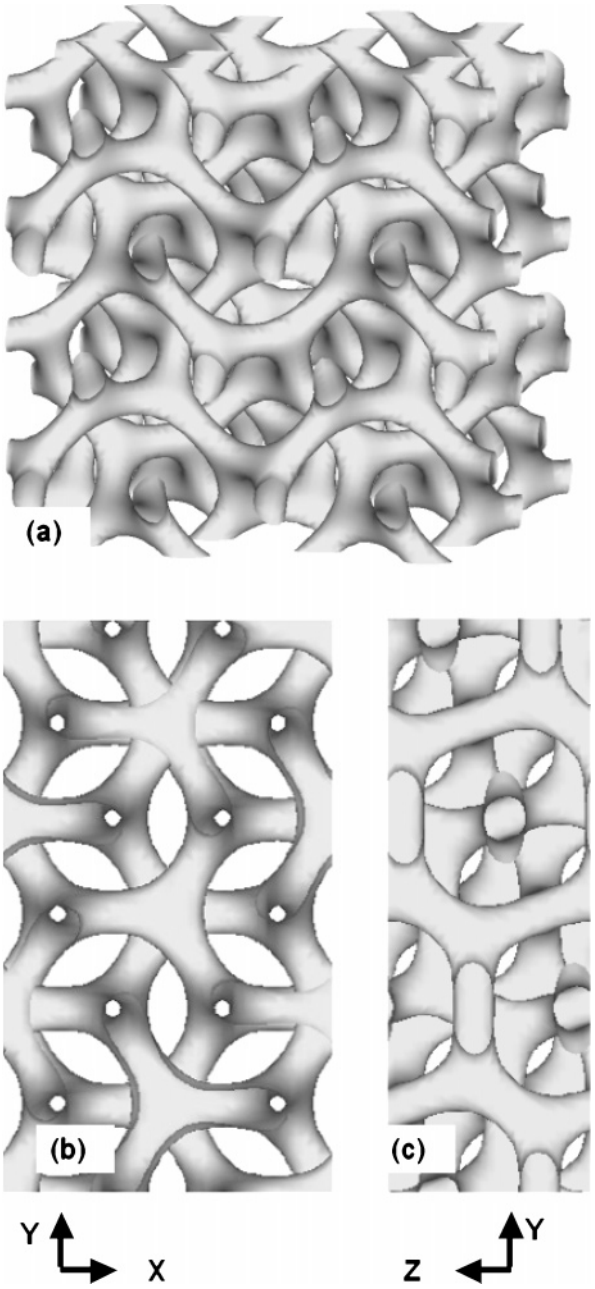

Figure 1. Bicontinuous double gyroid structure calculated using the SCF theory with SSO for $\chi N = 20$ and the block ratio $f = 0.35$. (a) Isosurfaces with $\phi = 0.9$ that enclose the minor phase ($2 \times 2 \times 2$ conventional unit cells) are shown, where ϕ is the local volume fraction of the minor phase. (b) Isosurfaces with $\phi = 0.75$ of the same structure viewed from the [111] direction of the original unit cell in (a) are shown. (c) Similar to (b), but along the $[1\bar{1}0]$ direction.

process is highly dependent on the dynamics of the domain structures, whose time and length scales are often beyond the resolution of the scattering experiments.[26−30] For example, in the case of OOT G ↔ C, the positions and the lattice constant of the created cylindrical domains are believed to be in commensurate to those of the original G domains. In Figure 2, two possible sets of the positions of the generated C domains are shown on the projection of the original G structure onto the [111] direction of the conventional unit cell. Figure 2a is the case where the {10} planes of the C domains are commensurate with the {112} planes of the G domains, while in Figure 2b, the {10} planes of the C domains are commensurate with the {220} planes of the G structure. For simplicity of notation, we

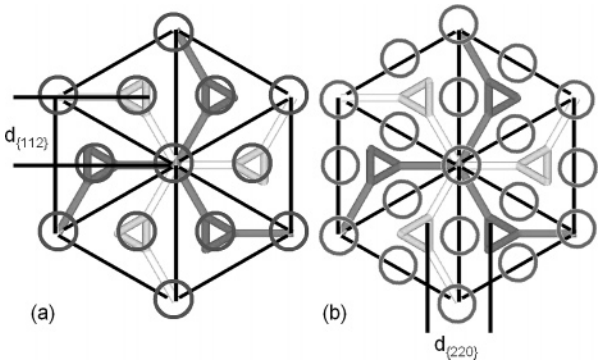

Figure 2. Projection of the G unit cell structure observed from the [111] direction.[29] The circles indicate the positions of the cylindrical domains in the epitaxial transition (a) G {211} → C {10} and (b) G {220} → C {10}, respectively.

hereafter denote these transitions as C {10} → G {112} and C {10} → G {220}, respectively.

Upon a temperature change, Rançon and Charvolin have observed the C {10} → G {211} in a hexaethylene glycol monododecyl ether/H_2O system.[26] On the other hand, Schulz et al. have reported a different epitaxial relationship C {10} → G {220} in a poly(styrene)-poly(2-vinylpridine) mixture under a shear flow and a temperature change.[27]

Most of the existing experiments[28−30] and theories[18,23,25] support the OOT C {10} ↔ G {211}. However, the details of the microscopic dynamics of this epitaxial transition have never been observed directly due to the limitation in the resolution of the scattering experiments. The same is true for the theoretical situations because most of the theoretical works have been done by using the representations in the reciprocal lattice space, which are not suitable to treat the nucleation and growth process in the first-order phase transition. Actually, an existence of a stable boundary between the C and G phases has been suggested by experimental observations on a poly(isoprene-*b*-ethylene oxide) diblock copolymer melt[31] and on a poly(styrene-*b*-isoprene) diblock copolymer solubilized in a dialkyl phthalates solvent.[32] To investigate the dynamics of such spatially inhomogeneous structures, a dynamically extended SCF simulation in real space is the most suitable technique.[33−37]

In the present work, we study the dynamics of the morphological change of the domains in the OOT G → C induced by a shear flow by using real-space computer simulations based on a dynamical extension of the SCF theory. Our target process OOT G → C shares many common characteristic features with the other OOTs, such as the epitaxial domain growth, the first-order transition, the strong effect of the external flow, and the coupling between the domain deformation and the change in the chain conformation. Therefore, studying this particular type of the OOT process is expected to give us general and useful information on the dynamics of the OOTs of block copolymers.

We are especially interested in the microscopic dynamics of the domains in the transition process and how important the epitaxial conditions are shown in Figure 2, the directions of the shear flow and its velocity gradient are. For example, in Figure 2, the directions of the two planes G {112} and G {220} are perpendicular with each other and the spacings between adjacent planes are different for these two cases. Actually, the spacing of the G {220} planes is closer to the equilibrium spacing of the C {10} planes than that of the G {211}. Therefore, the system should select OOT G {220} ↔ C {10} if the matching of the lattice spacings is the most dominant factor. How such an epitaxial condition affects the morphological change of the domains at a grain boundary between the G

phase and the C phase should be clarified in order to understand the OOTs correctly. Another candidate for the dominant factor in determining the OOT mechanism is the direction of the velocity gradient of the shear flow. This direction considerably affects the stability of the grain boundary between different domain structures, where the splitting and reconnection of domains take place steadily. Such steady splitting and reconnection of domains lead to a different transition mechanism than the scenario proposed by Matsen,[25] where the 3-fold junctions transform into 5-fold junctions and the epitaxial OOT G {211} ↔ C {10} is supported. Actually, we will see that the OOT is determined as a result of the competition between the epitaxial condition and the direction of the velocity gradient.

Because the lattice spacing changes slightly upon the phase transition, the use of the usual simulation box with a fixed size is not suitable. To eliminate this difficulty, we introduce a system size optimization (SSO) method, in which the side lengths of the simulation box are automatically adjusted so that the size and the shape of the simulation box are fit for the lattice spacing and the lattice axes of the ordered structures. Recently, a similar technique has been proposed by Bohbot-Raviv and Wang[38] and also by Barrat et al.[39] to study equilibrium domain morphologies of block copolymer systems. We adopt such SSO technique to the dynamical problems after carefully checking the validity of the method.

Apart from this SSO method, the way we introduce the dynamics of the domains is a rather simple one based on the local diffusion process of the segments driven by the gradient of the chemical potential. There are several advanced treatments of the dynamics in the SCF theory, where the Rouse dynamics or the reputation dynamics of the conformations of the constituent polymer chains are taken into account.[40−42] Along with such chain dynamics, the hydrodynamic interaction should also be taken into account. This can be done by solving the viscoelastic flow equation with the constitutive equation.[43] Such a detailed treatment will be necessary when the characteristic time scale of the shear deformation is shorter than or on the same order as the relaxation time of the chain conformation. However, the use of such advanced techniques is beyond the scope of this work, and we will limit ourselves to the slow shear deformation region where the splitting and reconnection processes of the domains play the dominant role in the transition. For this purpose, we use the "Simulation Utilities for Soft and Hard Interfaces (SUSHI)" in the OCTA system.[44]

2. Theory

2.1. Dynamical Self-Consistent Field Theory with a Shear Flow. Here, we give a brief description of the dynamical SCF theory used in the present study, focusing on our special extensions. For the details, readers should refer to Appendix A. Our system is a melt of a diblock copolymer composed of A-segments and B-segments. Within the mean-field approximation, the phase diagram of such a diblock copolymer melt is determined by two independent parameters: one is χN, where χ is the Flory−Huggins interaction parameter and N is the total number of segments composing the diblock copolymer, and the other is the block ratio $f = N_A/(N_A + N_B)$, where N_A and N_B are the numbers of segments composing the A and B subchains.[8]

For the dynamics, we assume a local equilibrium assumption that means only the local segment densities of individual components are the dynamical variables, and the other degrees of freedom, such as the chain conformations, are assumed to be in equilibrium under the constraint imposed by the local segment densities.[22,33−36] Let us denote the local segment density of the K-type (K = A or B) segment at time t as $\phi_K(\mathbf{r}, t)$. The self-consistent external potential $V_K(\mathbf{r})$ imposed on the K-type segments is decomposed into two contributions: one is the direct interaction potential imposed by the nearest-neighbor segments and the other is the constraining potential imposed by the segment density profile $\phi_K(\mathbf{r})$. It can be easily seen that the latter is a minus of the chemical potential for the K-type segments $\mu_K(\mathbf{r})$.[22] To obtain the chemical potential $\mu_K(\mathbf{r})$, one has to solve a set of self-consistent equations by using an iterative refinement method (See Appendix A).

We further assume that the flux of the segment density $\phi_K(\mathbf{r})$ is proportional to the gradient of the chemical potential $\mu_K(\mathbf{r})$. This is the Fick's law of linear diffusion. Then, the time evolution equation for the segment densities including the effect of the external flow is given as follows

$$\frac{\partial}{\partial t}\phi_K(\mathbf{r}, t) = L_K\nabla^2\mu_K(\mathbf{r}) - \nabla\cdot\{\mathbf{v}(\mathbf{r}, t)\phi_K(\mathbf{r}, t)\} \qquad (1)$$

where L_K is the mobility of a K-type segment, and $\mathbf{v}(\mathbf{r}, t)$ is the local flow velocity such as the velocity of the externally imposed shear flow.

2.2. System Size Optimization Method. Periodic microdomain structures of diblock copolymers have crystal symmetry. To obtain equilibrium states of these periodic structures using the mean-field theory, the free energy density of the system (refer to Appendix A) should be minimized with respect to the lattice structures of the ordered microdomains. The same is true for two phase coexisting states where the system size should be optimized with respect to the coexisting two periodic structures. For this purpose, we introduce the SSO method that minimizes the free energy density of the system by optimizing the side lengths of the simulation box on which periodic boundary conditions are imposed. This is a similar method to the constant pressure molecular dynamics simulation proposed by Andersen[45] and also by Parrinello and Rahman.[46]

2.2.1. Static System Size Optimization Method. In the static SCF calculations, this optimization can be performed by requiring the following local equilibrium condition for each side length of the simulation box[38]

$$\frac{\partial(\mathcal{F}/\mathcal{V})}{\partial\mathcal{L}_i} = 0 \qquad (2)$$

where $\mathcal{L}_i (i = x, y, z)$ is the side lengths of the simulation box, $\mathcal{F}$ is the total free energy, and $\mathcal{V}$ is the total volume of the system. The left-hand side of eq 2 can be evaluated numerically, as written in Appendix B.

2.2.2. Dynamical System Size Optimization Method. When the dynamical SCF calculation is performed, we should regard the side length of the simulation box $\mathcal{L}_i$ as a dynamical variable whose dynamics is described by the following fictitious equation of motion

$$\frac{\partial\mathcal{L}_i}{\partial t} = -\zeta_i\frac{\partial(\mathcal{F}/\mathcal{V})}{\partial\mathcal{L}_i} \qquad (3)$$

where ζ_i is a positive coefficient whose value is chosen properly so that the local equilibrium condition eq 2 for $\mathcal{L}_i$ is guaranteed at every time step.

We checked the validity of our dynamical SSO method by using a melt of an A−B diblock copolymer with the total number of segments $N = 20$, the block ratio of the A block $f = 0.35$, and the effective bond lengths of each segment type unity. The equilibrium phase of this block copolymer melt at $\chi N =$

15 is the C phase. As is described in detail in Appendix C, we found that the most appropriate value of the ζ_i is 0.05.

3. Simulation Results: The Epitaxial OOT from the G Structure to the C Structure

We simulated the epitaxial OOT G → C by imposing an external shear flow to an A−B diblock copolymer that is characterized by the parameters given in Section 2.2.2.

The initial state of the simulation is chosen as the equilibrium G structure at $\chi N = 20$. The co-continuous isosurfaces of the equilibrium G structure are shown in Figure 1a, which is composed of $2 \times 2 \times 2$ conventional G unit cells with cubic shape. From these conventional cells, we cut out a rectangular parallelepiped (not cubic) periodic cell, whose *Z*-axis is taken to be directed to the [111] direction of the original conventional G unit cell. The other two axes are selected so that the *X*-axis in $[1\bar{1}0]$ direction and the *Y*-axis is in the $[11\bar{2}]$ direction, respectively. We performed our OOT simulations by using this rectangular parallelepiped cell. The side length of the optimized conventional G unit cell is $D_G{}^0 = 17.2$ (in a unit of segment size that is taken to be unity), and the side lengths of the rectangular parallelepiped cell are $\sqrt{2}D_G{}^0$, $\sqrt{6}D_G{}^0$, and $(\sqrt{3}/2)D_G{}^0$, respectively, where the volume of the unit cell is three times larger than that of the cubic G unit cell, as shown in Figure 1b and c. The detailed technique used in preparing the initial G structure is summarized in Appendix D.

One way of inducing the OOT G → C is suddenly increasing the temperature from $\chi N = 20$ to $\chi N = 15$, the former and the latter corresponding to the G and C phases, respectively.[9] Such a phase transition is believed to be first order and should basically be initiated by a considerably large thermal fluctuation. Another way of inducing the transition is to impose an external flow field,[35] which considerably accelerates the transition. We introduce a shear flow whose flow direction is oriented to the *Z* direction ([111] direction) of the G unit cell. As long as the flow velocity is small compared to the relaxation time of the deformations of individual domains, the first-order nature of the OOT is preserved.[35] The Lees−Edwards boundary condition is employed in the direction of the velocity gradient of the shear flow,[47] while the periodic boundary conditions are employed in the other directions.

For the dynamical simulations, the following simulation parameters are used: the mobility L_K in eq 1 is set to $L_K = 1.0$, the shear rate $\dot{\gamma} = 0.001$, and the time mesh width $\Delta t = 0.01$, respectively. In the SCF iterations, if the difference between the two segment density fields at consecutive iteration steps becomes everywhere below $\Delta\phi = 0.0005$, we regard the segment density field has converged. We used two types of shear flows that have different directions of the velocity gradient: one is in the *X* direction ($[1\bar{1}0]$ direction) and the other is in the *Y* direction ($[11\bar{2}]$ direction).

3.1. The Epitaxial OOT under a Shear with a Velocity Gradient in the *Y* Direction ($[11\bar{2}]$ Direction).

3.1.1. Without the SSO Technique. First, we discuss the case with the shear velocity field $\mathbf{v}(\mathbf{r})$ with the flow in the *Z* direction and the shear gradient in the *Y* direction defined by

$$\mathbf{v}(\mathbf{r}) = \left(0, 0, \dot{\gamma}\left(\frac{\mathscr{L}_y}{2} - y\right)\right) \tag{4}$$

where *y* is the Cartesian coordinate along the *Y* axis and the $\mathscr{L}_y/2$ is the *Y* coordinate of the center of the system. The parameter ζ_i for the SSO is set at 0.05, as was discussed in Appendix C. Using this parameter, the SSO is performed at every other 100 time steps.

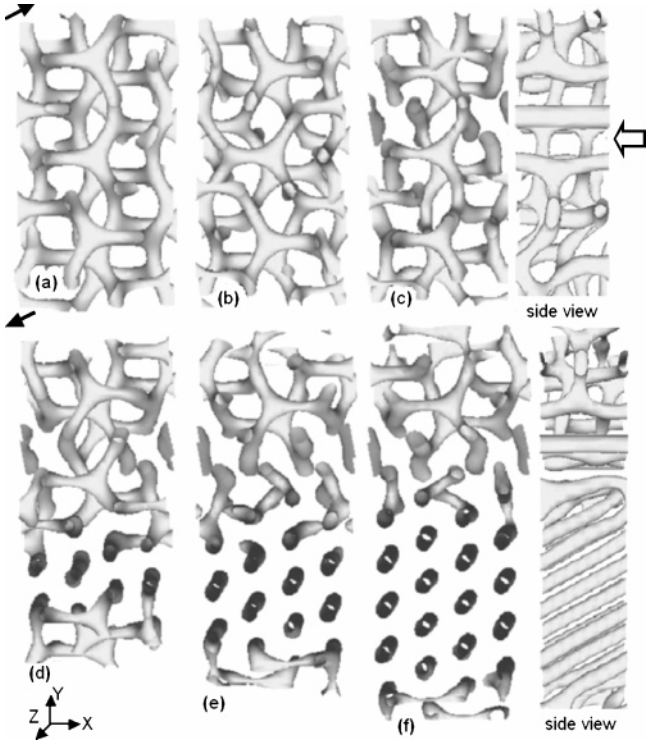

Figure 3. Time evolution of the domain in the epitaxial OOT G → C simulated with SSO is shown. A shear flow is imposed in the [111] direction of the G unit cell with $\dot{\gamma} = 0.001$. The directions of the shear flow are shown by black arrows. The viewpoint of the graphics is set so that one can verify the growth of the C structure. The snapshot figures are taken at times t = (a) 100, (b) 960, (c) 1960, (d) 3960, (e) 4960, and (f) 5960, respectively. For the cases (c) and (f), we also show the side views, where the white arrow indicates the stable grain boundary where cylindrical domains parallel to the shear direction ([111] direction) are generated.

The temporal change of the microphase domain structure is shown in Figure 3. The G structure is deformed by the shear flow, as shown in Figure 3a and b. Suddenly, a small domain of cylinders is generated in Figure 3c, which is indicated by an open arrow. The cylinders in this domain are parallel to the [111] direction of the G unit cell. The transition from the G structure to the C structure takes place at the lower grain boundary of this C domain, as shown in Figure 3d−f. It is characteristic that the cylinders are not completely parallel to the [111] direction of the G unit cell but are tilted with a certain angle, as shown in the side view of Figure 3f. This situation is different from the previous simulations by Zvelindovsky et al., where a much faster shear flow is imposed.[35] The tilting of the cylinders is caused by the steady splitting and reconnecting of the cylindrical domains, as will be discussed in Section 3.2.

Three-fold junctions in the upper G phase shown in Figure 3f are stable and are migrated by the shear flow. Even in the late stage of the simulation ($t = 10000$), we cannot obtain the perfect C structure and the coexistence between the C phase and the G phase is stable.

3.1.2. Without the SSO Technique. To check the effect of the SSO method, we carried out the same dynamical SCF simulation as in Section 3.1.1 but without the SSO method. The time evolution of the domain morphology is shown in Figure 4. In this case, as shown in Figure 4a−d, the OOT occurs at the center of the system where the G structure transforms into the C structure. The stable grain boundary, as shown in Figure 3, is, however, not observed in this case without SSO. The

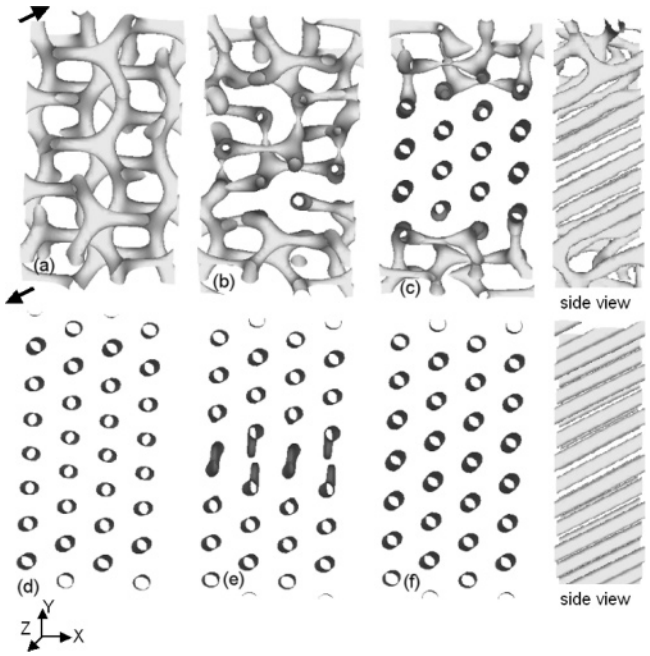

Figure 4. Similar to Figure 3, but without SSO.

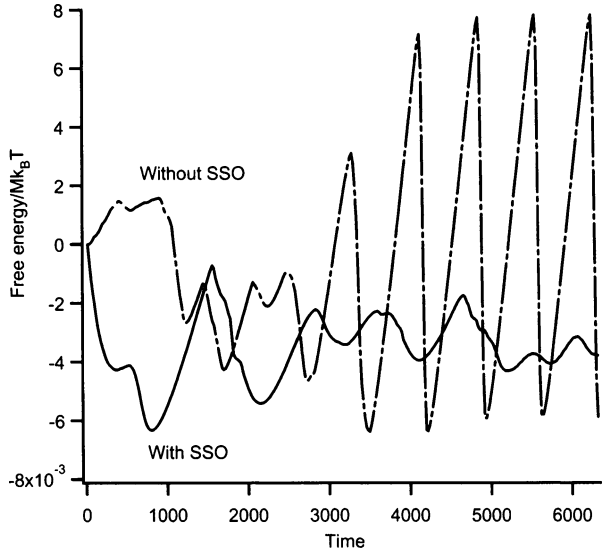

Figure 5. Time evolutions of the free energy per polymer chain with SSO and without SSO during the phase transition are shown. In both of these cases, the initial value of the free energy is set to be zero.

cylindrical domains are also tilted to the [111] direction of the G unit cell, as is shown in the side view of Figure 4c. After such a transient state, the system reaches the complete C structure. A characteristic phenomenon is observed near the center of the system where the cylindrical domains reconnect, as shown in Figure 4d−f. Such reconnections continue steadily for a certain time duration. This reconnection phenomenon means that the system is in a dynamical steady state where the energy injected by the shear flow into the system is released by the energy dissipation accompanied by the periodic reconnections of the cylindrical domains.

3.1.3. Time-Dependent Profiles of the Free Energy Density and the System Size. To compare the stability of the system for the individual cases with and without the SSO, we plot in Figure 5 the time evolution of the free energy density during the phase transition. The free energy density in the case with the SSO shows small periodic oscillations. On the other hand, in the case without the SSO, the system shows strong oscillations synchronized to the reconnections of the cylindrical domains. Such a periodic change in the free energy density is observed after $t = 3000$, when the system reaches the almost perfect C structure without defects. To obtain such a perfect C phase, the system goes over energy barriers with the aid of the driving force of the shear flow.

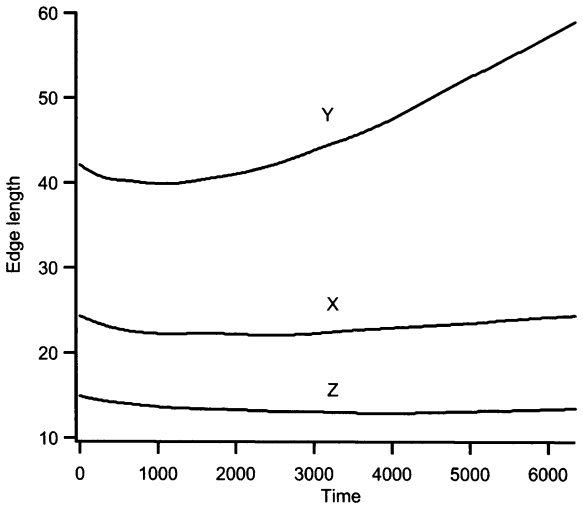

Figure 6. Time evolutions of the side lengths of the simulation box during the phase transition are shown.

Thus, in the case without SSO, the energy barrier should be much higher than the case with SSO because the constant system size imposes a severe restriction on the reconnection of the cylindrical domains. In the case with SSO, such a restriction is avoided by the change in the side length of the simulation box in the *Y* direction, as shown in Figure 6, which shows the time-dependent profile of side lengths of the simulation box with the SSO. The side lengths in the *X* and *Z* directions are almost constant, which means that the epitaxial condition is satisfied. Note that all three side lengths of the simulation box are a smooth function of time. They do not oscillate as the free energy density does. This means the temporal change in the size of the simulation box is slow enough that the local equilibrium condition is not violated.

3.2. The Epitaxial OOT under a Shear with a Velocity Gradient in the *X* Direction ([1$\bar{1}$0] Direction). We also tried simulations under a shear flow whose velocity gradient is set parallel to the *X* direction ([1$\bar{1}$0] direction). In this case, the free energy of the system increases slightly, but the nucleation and growth of cylindrical domains cannot be observed, even in the late stage $t = 6000$, either with SSO or without SSO. (Figures not shown.) Three-fold junctions perpendicularly oriented to the [111] direction of the G unit cell continue to disconnect and reconnect due to the shear flow. This result indicates that the G structure has different stabilities to different directions of the shear velocity gradient.

Figure 7 shows how the disconnection and the reconnection process takes place. The circles in the Figure 7 indicate the 3-fold junctions, where the disconnections and the reconnections take place. Figure 7a shows the structure after the disconnections, where we can observe the remains of 3-fold junctions indicated by the circles. Figure 7b shows the structure after the reconnections, where the 3-fold junctions regenerated.

The reason for these different stabilities depending on the different velocity gradient directions is explained by using Figure 8, which shows 3-fold junctions observed from the [111] direction of the G unit cell. The directions of the shear gradient are shown by the arrows beside each figure. Figure 8a shows a

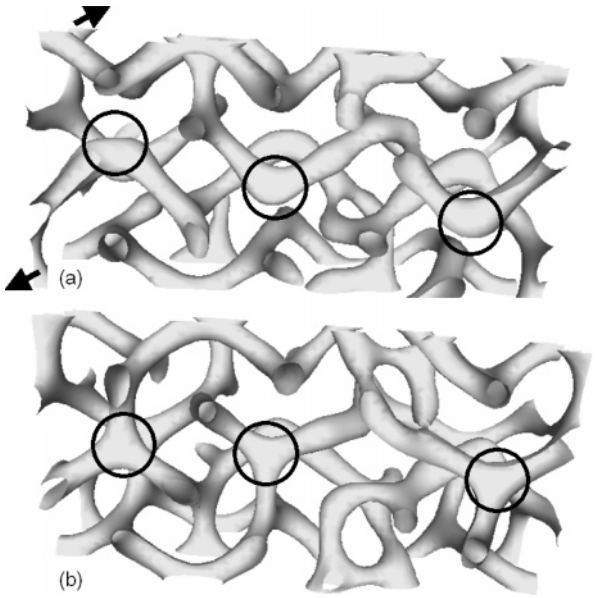

Figure 7. Time evolution of the G domain under a shear flow with its velocity gradient in the *X* direction and with $\dot{\gamma} = 0.001$. The circles indicate the three-fold junctions perpendicularly oriented to the [111] direction of the G structure. (a) Three-fold junctions are disconnected at $t = 3600$. (b) Three-fold junctions are regenerated at $t = 4200$.

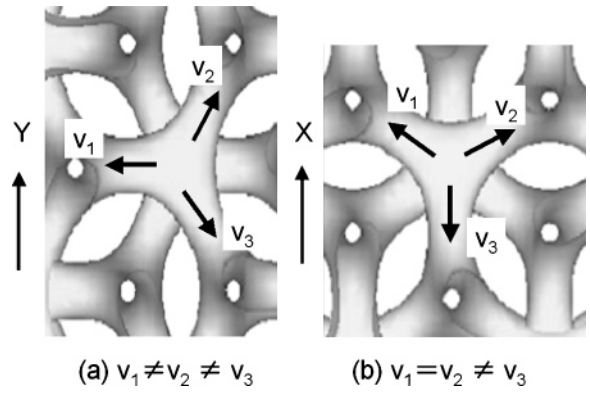

Figure 8. Three-fold junctions are migrated to different directions by the shear flow. (a) Under a shear flow with velocity gradient in the *Y* direction, and (b) a shear flow with velocity gradient in the *X* direction. In these two cases, the domains migrate in different manners.

3-fold junction under a shear flow with its velocity gradient in the *Y* direction. The three domains extending from the center of the 3-fold junction are subjected to different shear flow velocities, i.e., the three domains do not move with the same velocity v_y. Thus, the three domains are elongated to the different directions with different velocity, and the elongation finally makes the 3-fold junction disconnected. On the other hand, in the case of a 3-fold junction under a shear flow with its velocity gradient in the *X* direction, as shown in Figure 8b, two domains have the same velocity v_x. In this situation, the 3-fold junction is elongated to the direction of the *X*-axis. Even after the disconnection, two of the three domains keep connected and will be reconnected to another domain extending in the *X* direction to form the 3-fold junction structure again, as shown in Figure 7.

4. Discussions

4.1. Nucleation and Growth. Our simulation showed that the epitaxial OOT G → C takes place in the [111] direction of the G unit cell and that the epitaxial relation for the G {220} → C {10} transition is achieved. The transition does not occur uniformly, as shown in Figures 3d−f and 4c, where a region of C phase nucleates and grows.

Especially with the SSO method, the clear boundary is generated between the G phase and the C phase, as is shown in Figure 3. Actually, a clear boundary between the G and C phases is observed in experiments.[31,32] Our simulation succeeded in reproducing these experimental results.

Despite the small system size, the SSO method enables us to obtain clear phase coexistence under shear flow. Therefore, we conclude that the dynamical SCF method with SSO is a useful and reliable dynamical simulation method.

4.2. Epitaxial Condition. If the G {211} → C {10} is realized under a shear flow with the velocity gradient in the *Y* direction ([11$\bar{2}$] direction), the cylinders are oriented within the sheared plane, i.e., the *XZ* plane. Thus, the friction generated by the reconnecting domains to the shear flow is expected to be smaller than that for the G {220} → C {10} case, where the cylinder planes are oriented perpendicularly to the sheared plane. In our simulations, however, the system prefers the pathway as G {220} → C {10}, as shown in Figures 3 and 4. On the other hand, from the viewpoint of the matching between the lattice constants, G {220} → C {10} is preferable than the G {211} → C {10}. Our simulation result (G {220} → C {10} rather than G {211} → C {10}) suggests the importance of the matching between the lattice constants of the initial and the final structures, and the direction of the velocity gradient is not an important factor in determining the direction of the C planes for the epitaxial transition.

Most of the experiments and simulations have reported the epitaxial OOT G {211} ↔ C {10}, which disagrees with our simulation result. A possible reason for this discrepancy is as follows. At the initial stage, a nucleus of C domain is generated in a matrix of the G domains. As our simulation shows, this nucleus should have the orientation G {220} → C {10} because of the matching of the lattice constants and the stability of the connection and reconnection process at the grain boundary. The use of the SSO corresponds to a slight compressibility in the local lattice structure of the generated C phase. In real systems, such a slight compressibility can be realized by slightly distorting the surrounding G matrix. However, as the C region grows, the effect of the compressibility becomes less effective and the C structure is deformed (maybe tilted) to generate the experimentally observed orientation of the C domains in order to make its lattice constant matched to the surrounding G structure. Such a microscopic process in the initial stage of the nucleation process is beyond the resolution of the scattering experiments. Moreover, the usual TDGL simulations and the dynamical SCF simulations adopt the fixed simulation box and very often adopt the reciprocal lattice representation. In such simulations, the system will choose to go over a higher potential barrier rather than to trace the pathway shown in our simulation because such a pathway with lower potential barrier is forbidden due to the strict incompressibility.

4.3. Kinetic Pathway Model of the Epitaxial OOT G → C. Although the detail of the transition process is complex, we understand that the 3-fold junctions with domains perpendicular to the [111] direction of the G unit cell do not play an important role in the transformation from G to C. In our simulation, we observe that the 3-fold junctions are simply disconnected and vanish during the phase transition. This observation does not agree with the model of the epitaxial transition proposed by Matsen,[25] where a 3-fold junction is connected to one of the

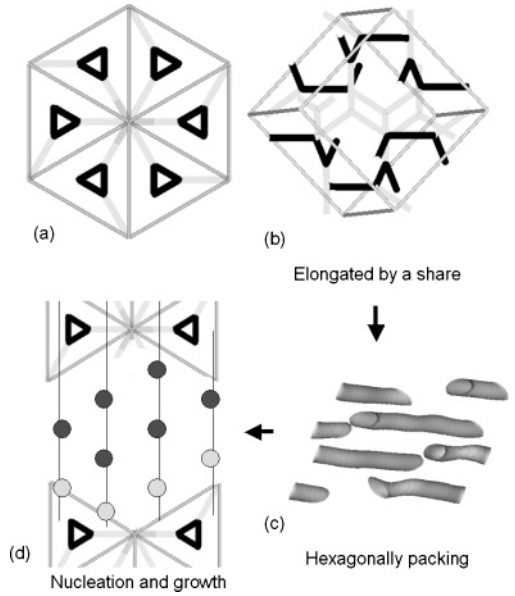

Figure 9. Model of the kinetic pathway of the epitaxial OOT G → C is illustrated. (a) Shown is the view of the G unit cell along the [111] direction, where the black domains transform to the C domains. (b) Another view of the same G unit cell as in (a) from a different direction is shown. (c) Image of the transformation from the elongated domains to the cylinders is shown. (d) Positions of the rearranged cylinders with hexagonal order are shown, where the lattice spacings satisfy the epitaxial relations G $d_{\{220\}}$ → C $d_{\{10\}}$.

nearest-neighbor 3-fold junctions to form a 5-fold junction. In our observation, 3-fold junctions are stable and they are not connected to any other junctions.

Here, we propose a model of the kinetic pathway. Figure 9a shows a projection of the G unit cell along the [111] direction, where the bold triangles are the projections of the consecutive three domains. Figure 9b is the same structure as Figure 9a, observed from a different direction. We can confirm that the triangles in Figure 9a are formed by the consecutive three domains (shown in black) connected by 3-fold junctions. When a shear flow is imposed, these black domains are elongated and form cylinders, as shown in Figure 9c, while the other domains shrink because they are strongly tilted to the flow velocity direction. These cylinders are rearranged to form a hexagonally packed cylindrical structure whose lattice spacings satisfy the epitaxial relations G {220} → C {10}, as shown in Figure 9d. This model of the kinetic pathway can be verified in Figures 3d−e and 4b−c.

4.4. The Effect of the Direction of the Velocity Gradient. We found that the dependence of the stability of the G domains on the direction of the shear gradient is caused by the different flow velocities imposed on the three domains meeting at a 3-fold junction, as shown in Figures 7 and 8. Such a microscopic explanation of the stability of the bicontinuous G domains against a shear flow has never been given. Our result demonstrates that the G structure is actually stable under a shear flow.

A naive consideration may lead to the expectation that the OOT G {211} → C {10} may take place for the case with the velocity gradient in the *X* direction because the lattice constant of the G structure in this case matches the lattice constant of the C structure more than the case with the velocity gradient in the *Y* direction. However, we cannot observe a transition even after a long simulation run. This suggests that the stability of the connection and reconnection process of the 3-fold junctions shown in Figure 8 is important in the OOTs.

5. Conclusion

The epitaxial OOT G → C was studied by using the real-space dynamical SCF technique with the SSO method. With such an SSO method, we succeeded in reproducing the realistic kinetic pathway of the first-order phase transition of G → C. On the other hand, in the absence of the SSO, we found that the kinetic pathway is very different from what we observed with SSO. We also found that the G structure shows different responses to different directions of the velocity gradient of the shear flow.

By using this technique, we studied the kinetic pathway of the G → C transition induced by a shear flow in the [111] direction of the unit cell of the G structure. We observed the following kinetic pathway: the G domains perpendicularly oriented to the [111] direction of the G unit cell do not contribute to the formation of the cylindrical domains. They are disconnected and vanish during the transition. On the other hand, the other G domains are elongated by the shear flow and transform into the cylindrical domains. Such deformations occur locally, and the cylindrical domains are rearranged to form a hexagonally close-packed C structure.

The most important result of our simulations with SSO is that we can observe a nucleation and growth of the C phase in the matrix of the G phase and a stable coexistence of these two phases, i.e., the nature of the first-order phase transition, which was not observed in the previous simulations done in the Fourier space. Under a steady shear flow, we observed that the G domains around the nucleus of the C phase deform and gradually join the C phase. We also observed that the domain spacing satisfies the epitaxial relationship G {220} → C {10} that is different from the experimental observations. We explain this discrepancy as a result of the different length and time scales between our simulation and the scattering experiments. Our simulation grasps the initial stage of the nucleation process.

As a conclusion, the dynamical SCF theory with the SSO method in real space is very useful and reliable to trace the OOTs and ODTs between the microdomain structures of block copolymer melts.

Acknowledgment. T.H. thanks H. Kodama and R. Hasegawa for the fruitful collaborations in coding SUSHI. The authors thank M. Doi (Tokyo University) and the members of the OCTA project for many helpful comments and discussions. They also thank M. W. Matsen, G. J. A. Sevink, T. Uneyama, and A. V. Zvelindovsky for valuable comments. This study is executed under the national project on nanostructured polymeric materials, which has been entrusted to the Japan Chemical Innovation Institute by the New Energy and Industrial Technology Development Organization (NEDO) under METI's Program for the Scientific Technology Development for Industries that Create New Industries. This work is partially supported by a grant-in-aid for science from the Ministry of Education, Culture, Sports, Science, and Technology, Japan. The computation was in part performed at the Super Computer Center of the Institute of Solid State Physics, University of Tokyo.

Appendix A. Self-Consistent Field Theory

In this appendix, we briefly summarize the SCF theory for an A−B diblock copolymer.[4,21,22,33] Let us consider a melt of A−B diblock copolymer. Because of the screening effect in the melts, we can assume Gaussian statistics for the chain conformation. Within these Gaussian statistics, the K-type (K = A or B) segment is characterized by the effective bond length b_K, and the K-type block is characterized by the number of

segments N_K. Then the total number of segments composing the block copolymer chain N is defined as $N \equiv N_A + N_B$. We introduce an index s to specify each segment, where $s = 0$ corresponds to the free end of the A block and $s = N$ corresponds to the other free end of the B block. Therefore, $0 \le s \le N_A$ and $N_A \le s \le N$ correspond to the A block and the B block, respectively. To evaluate the conformational entropy, we need the statistical weight of any subchains. Let us use the notation $Q(s', \mathbf{r}'; s, \mathbf{r})$ to denote the statistical weight of a subchain between sth and s'th segments ($0 \le s' \le s \le N$) that are fixed at the positions $\mathbf{r}$ and $\mathbf{r}'$. This statistical weight can be obtained by solving the following Edwards equation within the mean-field approximation

$$\frac{\partial}{\partial s}Q(s', \mathbf{r}'; s, \mathbf{r}) = \left[\frac{b(s)^2}{6}\nabla^2 - \beta V(s, \mathbf{r})\right]Q(s', \mathbf{r}'; s, \mathbf{r}) \quad (5)$$

where $\beta = 1/(k_B T)$, $b(s) = b_K$ if the sth segment is the K-type segment, and $V(s, \mathbf{r})$ is an external potential acting on the sth segment at $\mathbf{r}$ imposed by the surrounding segments and by the constraint on the segment density. Here, we assume that the external potential $V(s, \mathbf{r})$ is the same if the segment species (A or B) is the same. Thus,

$$V(s, \mathbf{r}) = \begin{bmatrix} V_A(\mathbf{r}) \text{ if } s \text{ indicates an A segment} \\ V_B(\mathbf{r}) \text{ if } s \text{ indicates a B segment} \end{bmatrix} \quad (6)$$

Equation 5 should be supplemented by the initial condition $Q(0, \mathbf{r}'; 0, \mathbf{r}) = \delta(\mathbf{r}' - \mathbf{r})$. As the two ends of the block copolymer are not equivalent, we should introduce another statistical weight $\tilde{Q}(s', \mathbf{r}'; s, \mathbf{r})$, which is calculated in the opposite direction along the chain starting from the free end $s = N$.

To reduce the computational cost, we define integrated statistical weights $q(s, \mathbf{r})$ and $\tilde{q}(s, \mathbf{r})$as follows:

$$q(s, \mathbf{r}) \equiv \int d\mathbf{r}' Q(0, \mathbf{r}'; s, \mathbf{r})$$

$$\tilde{q}(s, \mathbf{r}) \equiv \int d\mathbf{r}' \tilde{Q}(0, \mathbf{r}'; s, \mathbf{r}) \quad (7)$$

It is easy to confirm that $q(s, \mathbf{r})$ and $\tilde{q}(s, \mathbf{r})$ also satisfy eq 5.

By using eq 7, the density of the K-type segments at position $\mathbf{r}$ is given by

$$\phi_K(\mathbf{r}) = C \int_{s \in K-\text{block}} ds\, q(s, \mathbf{r})\, \tilde{q}(N - s, \mathbf{r}) \quad (8)$$

where C is the normalization constant:

$$C = \frac{\mathcal{V}}{\int d\mathbf{r} \int ds q(s, \mathbf{r})\, \tilde{q}(N - s, \mathbf{r})} = \frac{\mathcal{V}}{N\mathcal{Z}} \quad (9)$$

The parameter $\mathcal{V}$ is the total volume of the system and $\mathcal{Z}$ is the single chain partition function that is independent of K, i.e., $\mathcal{Z} = \int d\mathbf{r} q(s, \mathbf{r})\, \tilde{q}(N - s, \mathbf{r}) = \int d\mathbf{r} q(N, \mathbf{r}) = \int d\mathbf{r} \tilde{q}(N, \mathbf{r})$.

The external potential $V_K(\mathbf{r})$ can be decomposed into two terms as follows

$$V_K(\mathbf{r}) = \sum_{K'} \epsilon_{KK'}\phi_{K'}(\mathbf{r}) - \mu_K(\mathbf{r}) \quad (10)$$

The first term is the interaction energy between segments, where the $\epsilon_{KK'}$ is the nearest-neighbor pair interaction energy between a K-type segment and a K′-type segment that is related to the Flory−Huggins interaction parameter via $\chi_{AB} \equiv z\beta[\epsilon_{AB} - (1/2)(\epsilon_{AA} + \epsilon_{BB})]$ where z is the number of nearest-neighbor sites. The $\mu_K(\mathbf{r})$ is the chemical potential of the K-type segment, which is the Lagrange multiplier that fixes the density of the K-type segments at the position $\mathbf{r}$ to the specified density value. The $V_K(\mathbf{r})$ must be determined in a self-consistent manner so that this constraint is satisfied. Such a self-consistent condition is achieved by an iterative refinement of the $V_K(\mathbf{r})$.

To improve the stability of the numerical scheme, we used the following finite difference scheme for the Edwards equation, eq 5

$$q(s + \Delta s, \mathbf{r}) = \exp\left[-\frac{\beta V(s, \mathbf{r})\Delta s}{2}\right]\left(1 + \frac{b(s)^2}{6}\nabla^2 \Delta s\right) \exp\left[-\frac{\beta V(s, \mathbf{r})\Delta s}{2}\right] q(s, \mathbf{r}) \quad (11)$$

After the iteration is converged, the Helmholtz free energy of the system can be obtained as follows

$$\mathcal{F} = -k_B T M \ln \mathcal{Z} + \frac{1}{2}\sum_K \sum_{K'} \int d\mathbf{r} \epsilon_{KK'}\phi_K(\mathbf{r})\phi_{K'}(\mathbf{r}) - \sum_K \int d\mathbf{r} V_K(\mathbf{r})\phi_K(\mathbf{r}) \quad (12)$$

Appendix B. Numerical System Size Optimization Method

To evaluate the partial derivative in eqs 2 and 3, the following central difference scheme is used in the SSO mthod.

$$\frac{\partial(\mathcal{F}/\mathcal{V})}{\partial \mathcal{L}_i} = \frac{(\mathcal{F}/\mathcal{V})|_{(\mathcal{L}_i + \Delta\mathcal{L}_i)} - (\mathcal{F}/\mathcal{V})|_{(\mathcal{L}_i - \Delta\mathcal{L}_i)}}{2\Delta\mathcal{L}_i} \quad (13)$$

where $\Delta\mathcal{L}_i$ is a small variation of $\mathcal{L}_i$ and $(\mathcal{F}/\mathcal{V})|_{(\mathcal{L}_i \pm \Delta\mathcal{L}_i)}$ stands for free energy density $(\mathcal{F}/\mathcal{V})$ evaluated at $\mathcal{L}_i \pm \Delta\mathcal{L}_i$. We used the parabolic optimization method[48] to solve eq 2 in which we normalize the $\mathcal{L}_i$ by its initial value. The value of $\Delta\mathcal{L}_i$ is set to 10^{-6}, and the criterion of the convergence for the normalized $\mathcal{L}_i$ is set to 10^{-4}.

In the initial state, the spatial mesh is a simple cubic mesh. Even if the system size is changed by this SSO, the mesh structure is preserved. This means that the mesh is rectangular parallelepiped in the late stage of the simulations. The discretization of the partial differential equations for the SCF scheme is done by taking account of such a deformation of the mesh. We confirmed that different mesh sizes lead to the same result as long as the mesh size is small.

Appendix C. Test of the Dynamical System Size Optimization Method

To check the validity of the SSO method, we performed two-dimensional (2D) simulations on cylindrical domains. We set $L_K = 1.0$, $\zeta_x = \zeta_y = \zeta$ for simplicity, and the parameter Δs in eq 11 is taken as 0.2. The interaction parameter is set to be $\chi N = 15$, which corresponds to the C phase in its equilibrium state.[9] The initial state is set to the disordered phase to which we added small random noise with the standard deviation 0.0006. The initial shape of the simulation box is a square with side length 32.0. As the square shape of the simulation box is not compatible with the perfect C phase, the SSO method adjusts the side lengths of the simulation box automatically.

In Figure 10, we show a comparison of the domain morphologies in the late stage ($t = 5000$) between the two cases (a) with $\zeta = 0.001$ and (b) with $\zeta = 0.05$, respectively. In case (a), the C structure is distorted because the rate of the change in the side lengths of the simulation box is too slow to catch up with the change in the domain periodicity. On the other hand,

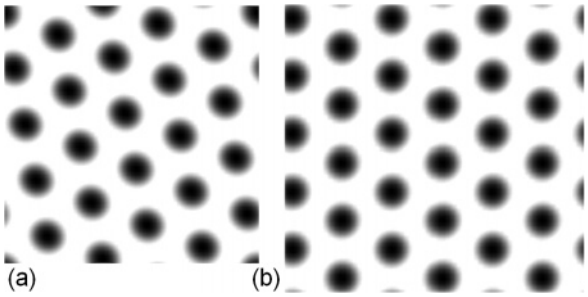

Figure 10. Comparison of the domain morphologies of an A−B diblock copolymer obtained with the 2D dynamical SCF simulations with SSO. Simulations were started form a D phase without the external flow. Model parameters are shown in the text. Values of the SSO parameter ζ are (a) $\zeta = 0.001$ and (b) $\zeta = 0.05$, respectively.

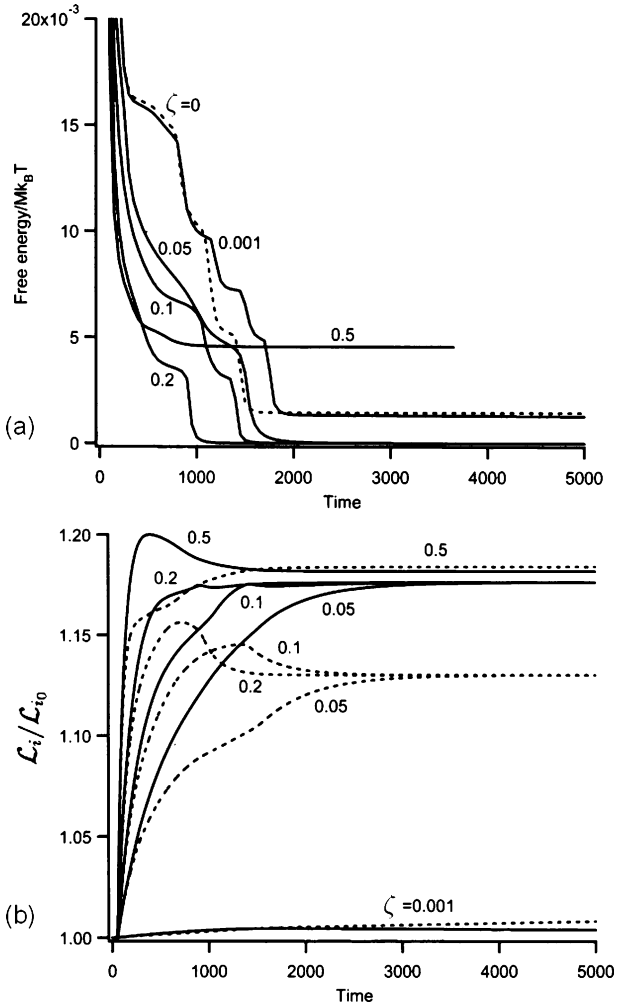

Figure 11. Time evolutions of the free energy per chain and side lengths for the C structure for several ζ values. (a) Time evolutions of the free energy per chain for the C structure are shown. The dotted curve is the result of the reference simulation with $\zeta = 0$. (b) Time evolutions of the side lengths of the simulation box. The solid and dotted curves show $\mathcal{L}_x$ and $\mathcal{L}_y$, respectively. Both side lengths are normalized by using their initial values $\mathcal{L}_{i0} = 32$ as $\mathcal{L}_i/\mathcal{L}_{i0}$.

in case (b), a perfect C phase is realized. When $\zeta = 0.5$, we observed that the dynamical scheme eq 3 becomes unstable.

Other dynamical variables that depend on the value of ζ are shown in Figure 11. Figure 11a shows the time evolution of the free energy. The dotted line is the reference state with $\zeta = 0$ (i.e., the case without SSO), which reaches the distorted morphology shown in Figure 10a. When the value of ζ is small ($\zeta = 0$ and 0.001), it takes a longer time for the free energy to relax, and finally, the system is trapped in a local minimum of the free energy. For the intermediate values of ζ ($\zeta = 0.05$, 0.1, and 0.2), the system reaches the perfect C phase, as shown in Figure 10b. When the value of ζ is large ($\zeta = 0.5$), the free energy initially drops rapidly and then the system is trapped by a local minimum of the free energy. These results mean that choosing an appropriate value of ζ accelerates the system to relax to the stable morphology without distortions and defects.

Figure 11b shows the time evolution of the side lengths of the simulation box. The solid curves and the dotted curves indicate the $\mathcal{L}_x$ and the $\mathcal{L}_y$, respectively. In all cases, the side lengths increase in the initial stage. After such an initial stage, the side lengths reach their maximum values and then decrease for large ζ value. When $\zeta = 0.05$, the curve does not show an overshoot, and the system smoothly reaches the perfect C phase. Thus, we judge that $\zeta = 0.05$ is the most appropriate value for our system.

Appendix D. Method of Generating the Initial G Structure

Let us denote the equilibrium (or steady-state) side length of the unit cell of the G structure as D_G, and the equilibrium (steady-state) spacing of the lamellar structure formed by the same block copolymer at $\chi N = 20$ as D_L. The value of D_L can easily be obtained by using a one-dimensional (1D) SCF calculation with SSO. Then, assuming an epitaxial relationship in the transitions L{10} → C {10} → G {211} at a fixed value of χN, we can obtain an approximant for D_G as follows

$$D_G = \sqrt{6} D_L \tag{14}$$

By using this value of D_G as the initial size of the simulation box, we set the SCF potential with the G symmetry as

$$V(x, y, z) = V_0\left(\cos\frac{2\pi x}{D_G}\sin\frac{2\pi y}{D_G} + \cos\frac{2\pi y}{D_G}\sin\frac{2\pi z}{D_G} + \cos\frac{2\pi z}{D_G}\sin\frac{2\pi x}{D_G}\right)^2 \tag{15}$$

where x, y, and z are the Cartesian coordinates, and the V_0 is an arbitrary small coefficient that we assume to be 0.001 for the minor component (segments composing the shorter subchain) and −0.001 for the major component (segments composing the longer subchain). An equilibrium G structure is obtained by a 3D static SCF calculation with this initial potential and SSO.

The equation in parentheses of eq 15 is called the "level-surface" of the G structure. The use of the squared form of the level-surface originates from the fact that the gyroid structure in block copolymer melt is formed by double networks, each with the G symmetry. By assigning different signs to the V_0's for major and minor components, we can let the minor phase gather inside the gyroid network, while the major phase becomes rich in the matrix region.

References and Notes

(1) Matsen, M. W.; Bates, F. S. *Macromolecules* **1996**, *29*, 1091−1098.
(2) Hamley, I. W. *Block Copolymers*; Oxford University Press: Oxford, 1999.
(3) Bates, F. S.; Fredrickson, G. H. *Physi. Today* **1999**, 52, 32−38.
(4) Fredrickson, G. H.; Ganesan, V.; Drollet, F. *Macromolecules* **2002**, 35, 16−39.
(5) Matsen, M. W. *J. Phys.: Condens. Matter* **2002**, *14*, R21−R47.
(6) Park, C.; Yoon, J.; Thomas, E. L *Polymer* **2003**, *44*, 6725−6760.
(7) Helfand, E.; Wasserman, Z. R. *Macromolecules* **1976**, *9*, 879−888. Helfand, E.; Wasserman, Z. R. *Macromolecules* **1978**, *11*, 960−966. Helfand, E.; Wasserman, Z. R. *Macromolecules* **1980**, *13*, 994−998.
(8) Leibler, L. *Macromolecules* **1980**, *13*, 1602−1617.
(9) Matsen, M. W.; Schick, M. *Phys. Rev. Lett.* **1994**, *72*, 2660−2663.

CDV

(10) Khandpur, A. K.; Foerster, S.; Bates, F. S.; Hamley, I. W.; Ryan, A. J.; Bras, W.; Almdal, K.; Mortensen, K. *Macromolecules* **1995**, *28*, 8796−8806.
(11) Hajduk, D. A.; Harper, P. E.; Gruner, S. M.; Honeker, C. C.; Kim, G.; Thomas, E. L.; Fetters, L. J. *Macromolecules* **1994**, *27*, 4063−4075.
(12) Alexander, C. E.; Augustine, M. U.; DeRege, P.; Chen, C. X.; Swager, T. M.; Hadjichristidis, N.; Xenidou, M.; Fetters, L. J.; Joannopoulos, J. D.; Fink, Y.; Thomas, E. L. *Adv. Mater.* **2001**, *13*, 421−425.
(13) Hashimoto, T.; Tsutsumi, K.; Funaki, Y. *Langmuir* **1997**, *13*, 6869−6872.
(14) Zhao, D.; Feng, J.; Huo, Q.; Melosh, N.; Fredrickson, G. H.; Chmelka, B. F.; Stucky, G. D. *Science* **1998**, *279*, 548−552.
(15) Chan, V. Z.-H.; Hoffman, J.; Lee, V. Y.; Iatrou, H.; Avgeropoulos, A.; Hadjichristidis, N.; Miller, R. D. *Science* **1999**, *286*, 1716−1719.
(16) Matsen, M. W.; Bates, F. S. *J. Chem. Phys* **1997**, *106*, 2436−2448.
(17) Qi, S.; Wang, Z. G. *Phys. Rev. Lett.* **1996**, *76*, 1679−1682. Qi, S.; Wang, Z. G. *Phys. Rev. E* **1997**, *55*, 1682−1697. Qi, S.; Wang, Z. G. *Polymer* **1998**, *39*, 4639−4648.
(18) Nonomura, M.; Ohta, T. *J. Phys. Soc. Jpn.* **2001**, *70*, 927−930. Nonomura, M.; Ohta, T. *Physica A* **2002**, *304*, 77−84. Nonomura, M.; Ohta, T. *J. Phys.: Condens. Matter* **2003**, *15*, L423−L430.
(19) Yamada, K.; Nonomura, M.; Ohta, T. *Macromolecules* **2004**, *37*, 5762−5777.
(20) Hong K. M.; Noolandi, J. *Macromolecules* **1981**, *14*, 727−736.
(21) Fleer, G. J.; Cohen Stuart, M. A.; Scheutjens, J. M. H. M.; Cosgrove, T.; Vincent, B. *Polymers at Interfaces*; Chapman & Hall: London, 1993.
(22) Kawakatsu, T. *Statistical Physics of Polymers: An Introduction*; Splinger-Verlag: Berlin, 2004.
(23) Laradji, M.; Shi, A.-C.; Noolandi, J.; Desai, C. R. *Macromolecules* **1997**, *30*, 3242−3255.
(24) Matsen, M. W. *J. Chem. Phys.* **2001**, *114*, 8165−8173.
(25) Matsen, M. W. *Phys. Rev. Lett.* **1998**, *80*, 4470−4473.
(26) Rançon, Y.; Charvolin, J. *J. Phys. Chem.* **1988**, *92*, 2646−2651.
(27) Schulz, M. F.; Bates, F. S.; Almdal, K.; Mortensen, K. *Phys. Rev. Lett.* **1994**, *73*, 86−89.
(28) Förster, S.; Khandpur, A. K.; Zhao, J.; Bates, F. S.; Hamley, I. W.; Ryan, A. J.; Bras, W. *Marcomolecules* **1994**, *27*, 6922−6935.
(29) Vigild, M. E.; Almdal, K.; Mortensen, K.; Hamley, I. W.; Fairclough, J. P. A.; Ryan, A. J. *Marcomolecules* **1998**, *31*, 5702−5716.
(30) Wang, C. Y.; Lodge, T. P. *Macromolecules* **2002**, *35*, 6997−7006.
(31) Floudas, G.; Ulrich, R.; Wiesner, U.; Chu, B. *Europhys. Lett.* **2000**, *50*, 182−188.
(32) Chastek, T. Q.; Lodge, T. P. *Macromolecules* **2003**, *36*, 7672−7680.
(33) Fraaije, J. G. E. M. *J. Chem. Phys.* **1993**, *99*, 9202−9212.
(34) Hasegawa, R.; Doi, M. *Macromolecules* **1997**, *30*, 5490−5493.
(35) Zvelindovsky, A. V.; Sevink, G. J. A.; van Vlimmeren, B. A. C.; Maurits, N. M.; Fraaije, J. G. E. M. *Phys. Rev. E* **1998**, *57*, R4879−R4882. Zvelindovsky, A. V.; van Vlimmeren, B. A. C.; Sevink, G. J. A.; Maurits, N. M.; Fraaije, J. G. E. M. *J. Chem. Phys.* **1998**, *109*, 8751−8754. Zvelindovsky, A. V.; Sevink, G. J. A.; Fraaije, J. G. E. M. *Phys. Rev. E* **2000**, *62*, R3063−R3066. Zvelindovsky, A. V.; Sevink, G. J. A. *Europhys. Lett.* **2003**, *62*, 370−376.
(36) Morita, H.; Kawakatsu T.; Doi, M. *Macromolecules* **2001**, *34*, 8777−8783.
(37) Hamley, I. W.; Castelletto, V.; Mykhaylyk, O. O.; Yang, Z.; May, R. P.; Lyakhova, K. S.; Sevink, G. J. A.; Zvelindovsky, A. V. *Langmuir* **2004**, *20*, 10785−10790.
(38) Bohbot-Raviv, Y.; Wang, Z.-G. *Phys. Rev. Lett.* **2000**, *85*, 3428−3431.
(39) Barrat, J. L.; Fredrickson, G. H.; Sides, S. W. *J. Phys. Chem.* **2005**, *109*, 6694−6700.
(40) Shima, T.; Kuni, H.; Okabe, Y.; Doi, M.; Yuan, X.-F.; Kawakatsu, T. *Macromolecules* **2003**, *36*, 9199−9204.
(41) Mihajlovic, M.; Lo, T. S.; Shnidman, Y. *Phys. Rev. E* **2005**, *72*, 041801−1−26.
(42) Narayanan, B.; Pryamitsyn, V. A.; Ganesan, V. *Macromolecules* **2004**, *37*, 10180−10194.
(43) Jupp, L.; Kawakatsu, T.; Yuan, X.-F. *J. Chem. Phys.* **2003**, *119*, 6361−6372.
(44) Honda, T.; Kodama, H.; Roan, J.-R.; Morita, H.; Urashita, S.; Hasegawa, R.; Yokomizo, K.; Kawakatsu, T.; Doi, M. *SUSHI Users Manual*; OCTA: Nagoya, Japan, 2004; (http://octa.jp).
(45) H. C. Andersen *J. Chem. Phys.* **1980**, *72*, 2384−2393.
(46) Parrinello, M.; Rahman, A. *J. Appl. Phys.* **1981**, *52*, 7182−7190.
(47) Allen, M. P.; Tildesley, D. J. *Computer Simulation of Liquids*; Oxford University Press: New York, 1987.
(48) Press, W. H.; Teukolsky, S. A.; Vetterling, W. T.; Flannery, B. P. *Numerical Recipes in C*; Cambridge University Press: Cambridge, 1992.

MA052075Z